JACS
JOURNAL OF THE AMERICAN CHEMICAL SOCIETY
pubs.acs.org/JACS
Article

Tunable Charge Transport and Spin Dynamics in Two-Dimensional Conjugated Metal−Organic Frameworks

Yang Lu,[□] Ziqi Hu,[□] Petko Petkov, Shuai Fu, Haoyuan Qi, Chuanhui Huang, Yannan Liu, Xing Huang, Mingchao Wang, Peng Zhang, Ute Kaiser, Mischa Bonn, Hai I. Wang, Paolo Samorì, Eugenio Coronado,* Renhao Dong,* and Xinliang Feng*

Cite This: J. Am. Chem. Soc. 2024, 146, 2574−2582

ABSTRACT: Two-dimensional conjugated metal−organic frameworks (2D c-MOFs) have attracted increasing interest in electronics due to their (semi)conducting properties. Charge-neutral 2D c-MOFs also possess persistent organic radicals that can be viewed as spin-concentrated arrays, affording new opportunities for spintronics. However, the strong π-interaction between neighboring layers of layer-stacked 2D c-MOFs annihilates active spin centers and significantly accelerates spin relaxation, severely limiting their potential as spin qubits. Herein, we report the precise tuning of the charge transport and spin dynamics in 2D c-MOFs via the control of interlayer stacking. The introduction of bulky side groups on the conjugated ligands enables a significant dislocation of the 2D c-MOFs layers from serrated stacking to staggered stacking, thereby spatially weakening the interlayer interactions. As a consequence, the electrical conductivity of 2D c-MOFs decreases by 6 orders of magnitude, while the spin density achieves more than a 30-fold increase and the spin−lattice relaxation time (T_1) is increased up to ∼60 μs, hence being superior to the reference 2D c-MOFs with compact stackings whose spin relaxation is too fast to be detected. Spin dynamics results also reveal that spinless polaron pairs or bipolarons play critical roles in the charge transport of these 2D c-MOFs. Our strategy provides a bottom-up approach for enlarging spin dynamics in 2D c-MOFs, opening up pathways for developing MOF-based spintronics.

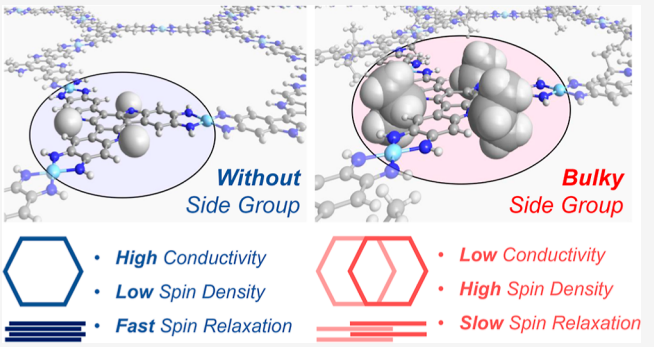

INTRODUCTION

Molecular systems with unpaired electrons have attracted increasing attention due to their exotic electronic and spintronic properties, which warrant their use in organic electronic devices and quantum information science (QIS).[1−8] Organic π-conjugated systems (particularly those with radicals) have long spin lifetimes and diffusion lengths due to their weak spin−orbit and hyperfine interactions.[9,10] These features endow organic π-conjugated radicals with longer coherence times including the spin−lattice relaxation (T_1) and spin−spin relaxation (T_2) times, which are critical temporal metrics for QIS.[1,11−13] However, organic π-conjugated radicals usually suffer from poor air stability. Thus, only limited organic molecules have been demonstrated for molecular spin-related applications.

When π-conjugated non-innocent organic ligands are linked to metal ions through redox coordination reactions, a new type of d-π conjugated van der Waals layered material, namely, two-dimensional conjugated metal−organic frameworks (2D c-MOFs), can be formed.[14−18] Unlike conventional MOFs, 2D c-MOFs are electrically conductive and can possess stable unpaired electrons located on organic conjugated moieties.[19−23] More importantly, these persistent spin centers are assembled into periodic arrays through in-plane square-planar secondary building units (SBUs) and out-of-plane π−π interactions.[24] Thus, 2D c-MOFs can be regarded as spin-concentrated molecular assemblies, offering the possibility to systematically optimize spin−lattice and spin−spin interactions compared to isolated organic conjugated molecules.[20] Nevertheless, the 2D c-MOFs usually prefer energetically favorable AA or AA-serrated stacking with strong interlayer interactions,[25−29] which lead to a reduced active spin density and accelerate spin−lattice relaxation and spin decoherence.[19,30] Hence, a rational design strategy to precisely tailor interlayer interactions, thus tuning the spin dynamics and enabling the long spin relaxation times in 2D c-MOFs, is highly sought after.

Received: October 9, 2023
Revised: January 5, 2024
Accepted: January 8, 2024
Published: January 17, 2024

https://doi.org/10.1021/jacs.3c11172
J. Am. Chem. Soc. 2024, 146, 2574−2582

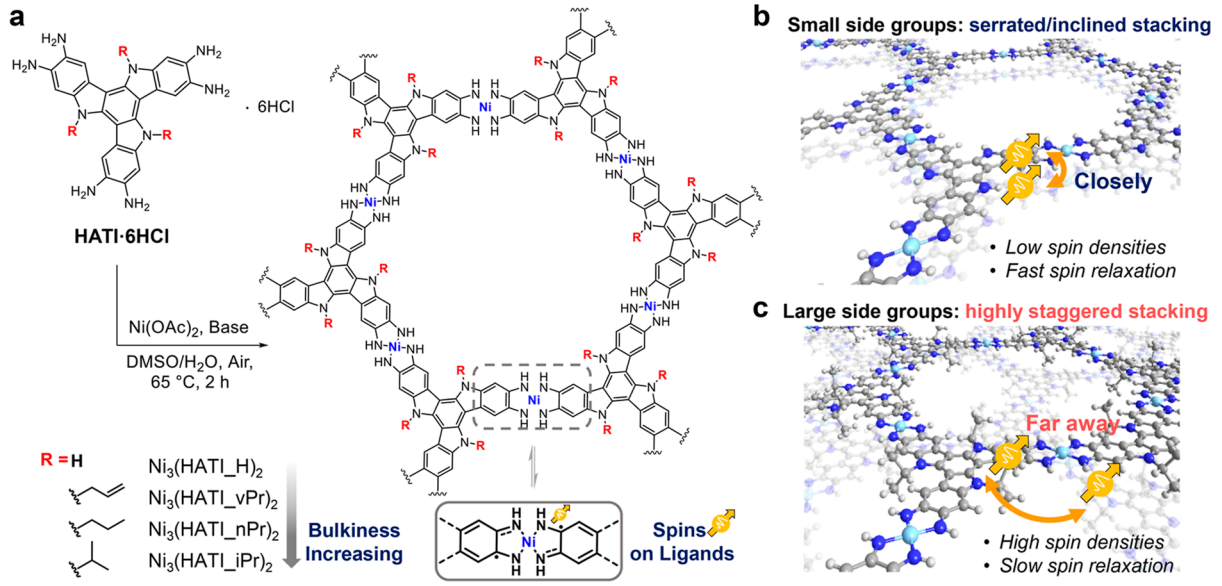

Figure 1. (a) Synthesis of $Ni_3(HATI\_X)_2$ 2D c-MOFs with the substitution of different side groups. The spin centers (yellow arrows) are located on the organic π-conjugated parts; (b,c) conceptual schematic for precise tuning of spin dynamics through control of stacking modes. (b) Serrated stacking or inclined stacking; (c) staggered stacking. Gray balls: C; white balls: H; blue balls: N; cyan balls: Ni.

Herein, we successfully achieve the tuning of the spin dynamics in 2D c-MOFs by introducing bulky side groups on the conjugated ligands. Various side groups with different sterically demanding groups grafted to π-conjugated 2,3,7,8,12,13-hexaiminotriindole (HATI) ligands, including hydrogen atom, allyl, n-propyl, and isopropyl groups (denoted as X = H, vPr, nPr, and iPr, respectively), which act as structural perturbation factors to tailor the stacking modes and the interlayer distances, thus affecting the interlayer interactions of the synthetic 2D c-MOFs [$Ni_3(HATI\_X)_2$, Figure 1a]. We show that the increase in the size of the bulky side groups leads to the widening of the interlayer spacings and a subsequent transition from serrated stacking to staggered stacking. Correspondingly, the electrical conductivities of these 2D c-MOFs are gradually diminished from 1 to 10^{-6} S cm^{-1}. However, because the distinct staggered packing drives the spin centers to be spatially isolated (Figure 1b,c), the resultant $Ni_3(HATI\_iPr)_2$ manifests an intrinsic spin density up to 5.96 × 10^{21} mol^{-1}, 30 times higher than that of $Ni_3(HATI\_H)_2$. Additionally, $Ni_3(HATI\_iPr)_2$ displays a significantly longer spin−lattice relaxation time (T_1, ∼60 μs), while the one of $Ni_3(HATI\_H)_2$ remains undetectable. The simultaneous realization of high spin densities and extended spin−lattice relaxation times is unprecedented among spin-concentrated assemblies. The spin dynamics studies also revealed the fact that the carrier transport in these 2D c-MOFs is dominated by spinless polaron pairs or bipolarons. Our work develops a bottom-up strategy for the controlled synthesis of layer-controlled 2D c-MOFs as spin arrays, opening interesting perspectives toward spintronic devices.

RESULTS AND DISCUSSION

Synthesis and Characterization. For the synthesis of HATI ligands without substituents, denoted as HATI_H, the *tert*-butoxycarbonyl (Boc) was introduced to protect the hexabromotriindole heterocycle and was removed in the last step (details are shown in the Supporting Information). The functionalization of hexaiminotriindole by substituents including allyl, n-propyl, and isopropyl groups was carried out through continuous nucleophilic substitution reaction, carbon−nitrogen coupling reaction, and deprotection, denoted as HATI_vPr, HATI_nPr, and HATI_iPr, respectively. Then, the reaction of HATI ligands with Ni^{2+} ions in a mixture of dimethyl sulfoxide (DMSO) and water at 65 °C for 2 h resulted in the 2D c-MOFs, $Ni_3(HATI\_X)_2$ (X = H, vPr, nPr, and iPr; details are shown in Figure 1a and Supporting Information). The use of spin-free nuclei ion, i.e., Ni^{2+}, to connect the HATI ligand scan generates organic radicals in conjugated ligands during the redox coordination reaction. The sodium acetate was also utilized as a weak base that could decrease the deprotonation and coordination reaction rate, which ensured high crystallinity of the final MOF product.

The high-resolution X-ray photoelectron spectroscopy (XPS) spectra in the Ni(2p) range evidence the presence of Ni(II) in all 2D c-MOFs (Figures S1 and S2). In addition, Na^+ peaks were not observed; the absence of extraneous cations suggested the neutral state of $Ni_3(HATI\_X)_2$. Fourier-transform infrared (FT-IR) spectra of $Ni_3(HATI\_X)_2$ reveal the disappearance of the stretch vibration band of the N−H groups from the ligand HATI_X (Figure S3), demonstrating efficient coordination polymerization between metal ions and conjugated ligands. Thermogravimetric analysis (TGA) reveals that all $Ni_3(HATI\_X)_2$ 2D c-MOFs start desolvation over 100 °C and exhibit pronounced weight losses above 200 °C due to decomposition (Figure S4). Scanning electron microscopy (SEM) and transmission electron microscopy (TEM) images reveal the formation of rodlike crystals of the 2D c-MOFs with domain sizes of 100−200 nm (Figures S5 and S6).

Structural Elucidation. The crystalline structures of 2D c-MOFs were determined by powder X-ray diffraction (PXRD) analysis with Cu Kα radiation. Figure 2a exhibits the PXRD patterns of all 2D c-MOFs under optimal synthesis conditions. As revealed from PXRD analysis, $Ni_3(HATI\_H)_2$ shows high crystallinity, exhibiting the first intense peak at a low angle of 3.7° (2θ), which corresponds to the (100) reflection plane, along with minor peaks at 6.4, 7.4, 9.8, 13.0, and 13.9°,

https://doi.org/10.1021/jacs.3c11172
J. Am. Chem. Soc. 2024, 146, 2574−2582

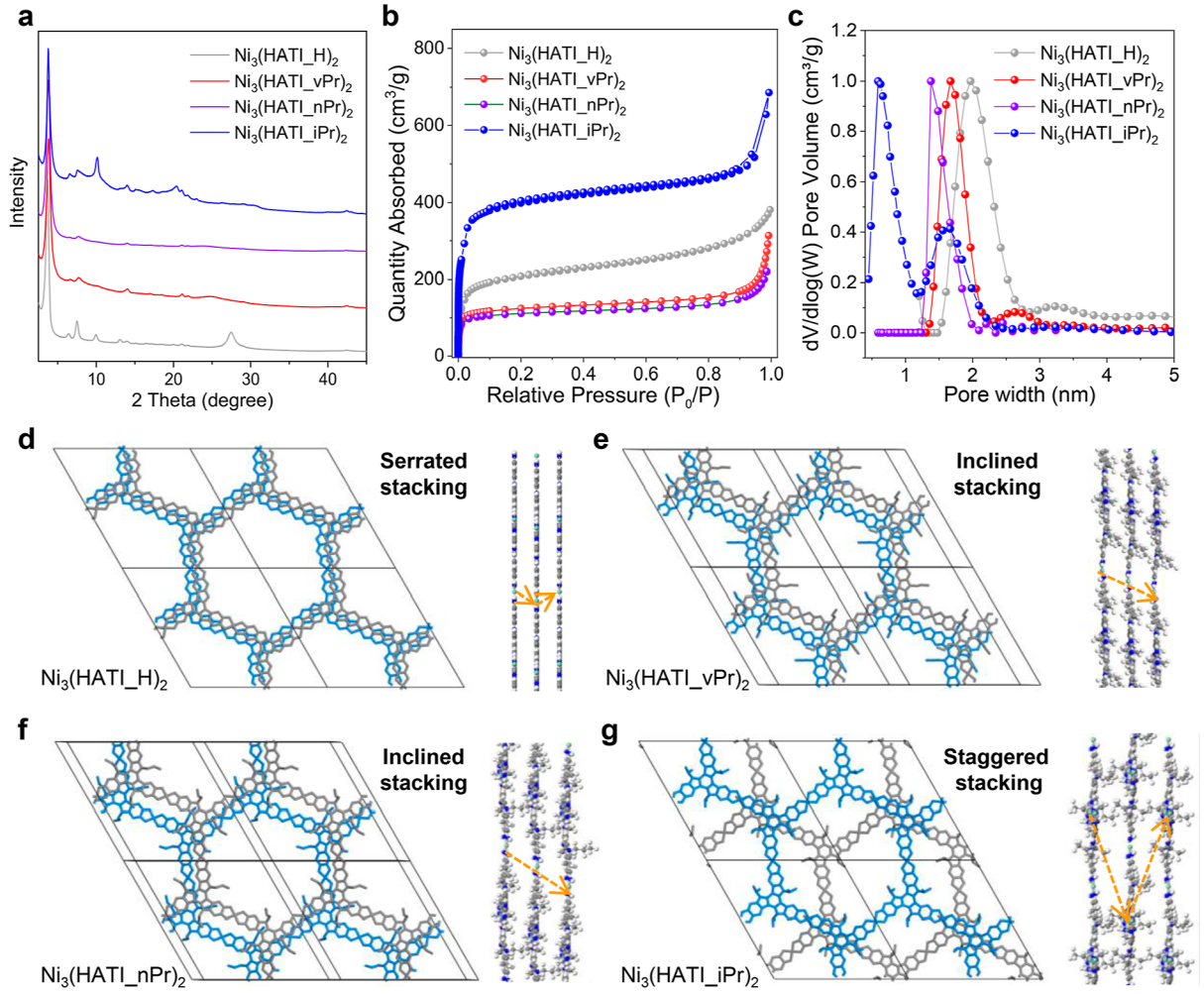

Figure 2. (a) XRD patterns for Ni3(HATI_H)$_2$, Ni$_3$(HATI_vPr)$_2$, Ni$_3$(HATI_nPr)$_2$, and Ni$_3$(HATI_iPr)$_2$. (b,c) N_2 adsorption isotherm and DFT pore distribution for Ni$_3$(HATI_H)$_2$, Ni$_3$(HATI_vPr)$_2$, Ni$_3$(HATI_nPr)$_2$, and Ni$_3$(HATI_iPr)$_2$, respectively. (d–g) Top (left) and side (right) views of the corresponding refined 2D crystal structures of Ni$_3$(HATI_H)$_2$, Ni$_3$(HATI_vPr)$_2$, Ni$_3$(HATI_nPr)$_2$, and Ni$_3$(HATI_iPr)$_2$, respectively.

attributable to the (110), (020), (210), (220), and (011) reflection planes, respectively. Ni$_3$(HATI_H)$_2$ shows an interlayer distance of about 3.21 Å, derived from the (002) peak at 27.5°. Ni$_3$(HATI_vPr)$_2$ and Ni$_3$(HATI_nPr)$_2$ exhibit similar PXRD patterns, which are ascribed to the same type of side chain substitution. For Ni$_3$(HATI_vPr)$_2$ and Ni$_3$(HATI_nPr)$_2$, the first and most intense peak corresponding to the (100) reflection plane appears at ~3.85°, with other minor reflections at 6.6, 7.7, and 14.0°, corresponding to the (110), (200), and (310) reflection planes, respectively. Due to the smaller steric bulkiness of the unsaturated allyl group, Ni$_3$(HATI_vPr)$_2$ displays a closer interlayer distance (3.58 Å) than the saturated propyl-substituted Ni$_3$(HATI_nPr)$_2$ (3.68 Å). It is notable that Ni$_3$(HATI_iPr)$_2$ exhibits strong PXRD peaks at 3.75, 6.5, 7.5, 10.1, 14.0, 20.4, and 21.1°, corresponding to the (100), (110), (2−20), (1−11), (211), (11−2), and (21−2) reflection planes, respectively, which are significantly different from the three samples mentioned. The huge steric bulkiness of the branching isopropyl group enables Ni$_3$(HATI_iPr)$_2$ to have the largest interlayer distance of around 4.70 Å among all of the achieved 2D c-MOFs, which also indicates significantly reduced interlayer interactions.

In order to elucidate the structures of Ni$_3$(HATI_X)$_2$ and calculate the unit cell parameters, a variety of possible stacking modes were considered and optimized by the density functional theory (DFT) method, including eclipsed stacking (AA), inclined stacking (AA-inclined), serrated stacking (AA-serrated), and staggered stacking (AB) models (Figure S7). Regarding Ni$_3$(HATI_H)$_2$ 2D c-MOF, the calculated AA-serrated stacking possesses the lowest total energy (at least lower by 275 kJ mol^{-1} per unit cell) compared with the other stacking modes, which also matches well with the experimental PXRD patterns (Figure 2d). For Ni$_3$(HATI_vPr)$_2$ and Ni$_3$(HATI_nPr)$_2$, the AA-inclined stacking model matches well with the experimental PXRD patterns (Figure 2e,f) and features the lowest total energy value (lower by 82−243 kJ mol^{-1} per unit cell) compared with AB, and AA-serrated stacking. In contrast to the common AA-serrated and -inclined stacking models mentioned above, the calculated staggered stacking (close to the AB model) agrees well with the PXRD patterns of Ni$_3$(HATI_iPr)$_2$ (Figure 2g). Pawley refinements offer optimized parameters that provide good consistency factors [R_p = 1.84% and R_{wp} = 5.79% for Ni$_3$(HATI_H)$_2$; R_p = 1.17% and R_{wp} = 1.91% for Ni$_3$(HATI_vPr)$_2$; R_p = 4.67% and R_{wp} = 7.66% for Ni$_3$(HATI_nPr)$_2$]. Similarly, unit cell

https://doi.org/10.1021/jacs.3c11172
J. Am. Chem. Soc. 2024, 146, 2574−2582

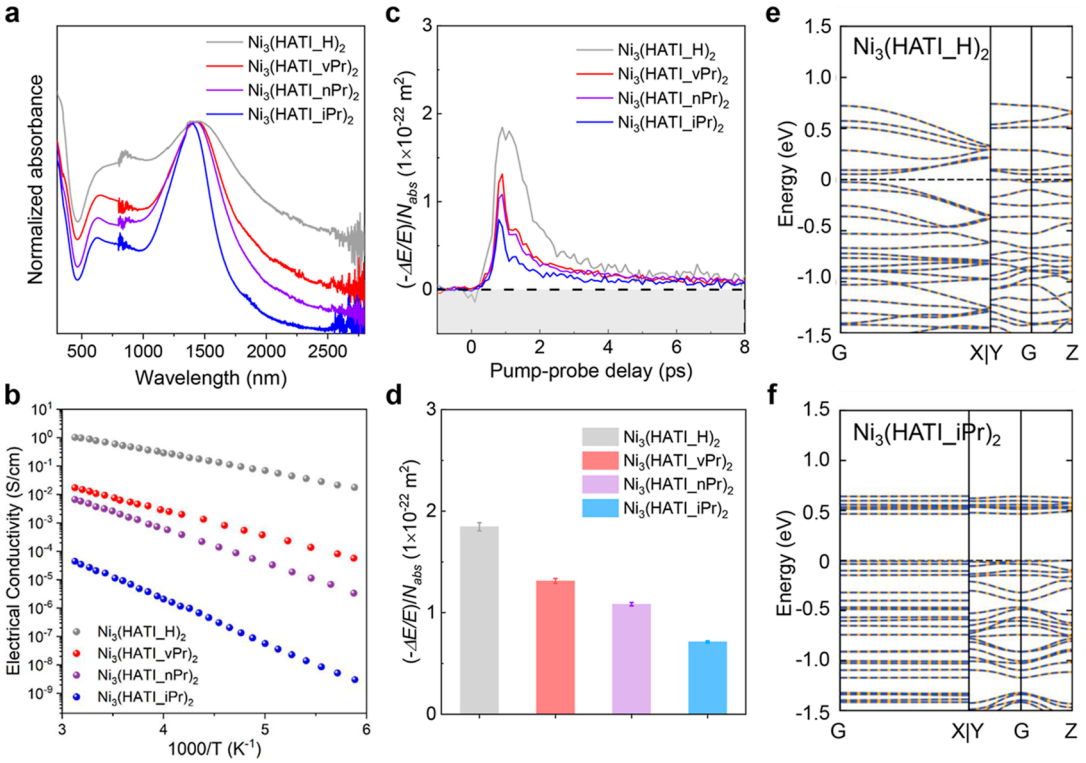

Figure 3. (a) Vis−NIR absorption spectra of $Ni_3(HATI\_X)_2$; (b) VT electrical conductivities of $Ni_3(HATI\_X)_2$; (c) THz photoconductivity dynamics of different samples normalized to the absorbed photon density (N_{abs}). The samples are photoexcited by an ultrashort pulsed laser (photon energy: 3.1 eV; absorbed fluence: 760 $\mu J/cm^2$); (d) comparison of the maximum THz photoconductivity of different samples normalized to N_{abs}. (e,f) Calculated band structures of bulk $Ni_3(HATI\_H)_2$ and $Ni_3(HATI\_iPr)_2$, respectively. The Fermi energy was set to 0 eV.

parameters are obtained for $Ni_3(HATI\_iPr)_2$ with acceptably low residuals (R_p = 2.54% and R_{wp} = 7.42%) (Figure S8).

N_2 sorption isotherms at 77 K on the activated 2D c-MOFs samples were measured to facilitate the structural elucidation and porosity investigation of side-group-functionalized 2D c-MOFs. Their adsorption curves exhibited a type-I adsorption isotherm (Figure 2b). The nonlocal density functional theory (NLDFT) gave rise to a narrow pore size distribution for $Ni_3(HATI\_X)_2$ (Figure 2c). $Ni_3(HATI\_H)_2$ exhibits a BET surface area of 788 $m^2 \cdot g^{-1}$ and 2.02 nm pore size. With the linear side chains grafted onto the pore walls, the BET surface areas of $Ni_3(HATI\_vPr)_2$ and $Ni_3(HATI\_nPr)_2$ were reduced as 472 and 411 $m^2 \cdot g^{-1}$, respectively, and the corresponding pore sizes were reduced as 1.66 and 1.40 nm. However, $Ni_3(HATI\_iPr)_2$ exhibits a significantly higher BET surface area of 1625 $m^2 \cdot g^{-1}$ compared to the other samples. The improvement in porosity of $Ni_3(HATI\_iPr)_2$ is evidenced by the *t*-plot pore area and *t*-plot pore volume, which are approximately 3 times higher than those of $Ni_3(HATI\_H)_2$ (Table S1), setting a new record among thus-far reported 2D c-MOFs.[14] Interestingly, the pore size distribution of $Ni_3(HATI\_iPr)_2$ evidenced two types of pores existing in this sample, with pore sizes of 1.60 and 0.60 nm, respectively, consistent with the simulated values for the highly staggered stacking mode (Figure 2g).[31,32]

Optoelectronic and Charge Transport Properties. Visible/near-infrared (vis−NIR) absorption spectroscopy indicates that all $Ni_3(HATI\_X)_2$ 2D c-MOFs present wide absorption bands in the near-infrared region, which are attributed to the organic radicals of the conjugated ligands after coordination with Ni ions (Figure 3a). As expected, the optical gaps estimated from the Tauc plots of $Ni_3(HATI\_X)_2$ reveal a significant increase from 0.26 to 0.46, 0.49, and 0.68 eV with increasing steric bulkiness of side groups and thus the interlayer distance (Figure S9). The staggered stacking of $Ni_3(HATI\_iPr)_2$ dramatically decreases the overlap of the frontier molecular orbital through the dislocating of the 2D layers and enlarging the layer spacing, leading to the large widening of the optical band gap, which further reveals the strong dependence of the electronic structure of 2D c-MOF on the stacking mode.

The electrical conductivities of $Ni_3(HATI\_X)_2$ were measured from the powder pellets by the collinear four-probe method under a vacuum in the dark. At 300 K, the electrical conductivity values were calculated as 1 ± 0.1, $(1 \pm 0.2) \times 10^{-2}$, $(4 \pm 0.7) \times 10^{-3}$, and $(2 \pm 0.4) \times 10^{-6}$ S cm^{-1} for $Ni_3(HATI\_H)_2$, $Ni_3(HATI\_vPr)_2$, $Ni_3(HATI\_nPr)_2$, and $Ni_3(HATI\_iPr)_2$, respectively. The electrical conductivities of $Ni_3(HATI\_X)_2$ span over 6 orders of magnitude, from reasonable to poor conductivity in the 2D c-MOFs (Figure S10). As shown in Figure 3b, all the samples present thermally activated charge transport according to the variable-temperature (VT) conductivity measurements from 200 to 320 K. The hopping activation energies were determined as 45, 190, 215, and 350 meV for $Ni_3(HATI\_H)_2$, $Ni_3(HATI\_vPr)_2$, $Ni_3(HATI\_nPr)_2$, and $Ni_3(HATI\_iPr)_2$, respectively, which correlate well with the bulk electrical conductivities and the calculated band gaps. To further investigate the microscopic transport properties of these 2D c-MOFs, we employed time-resolved terahertz spectroscopy (TRTS, see details in the Supporting Information). Briefly, an ultrashort pulse laser with 3.1 eV photon energy (400 nm wavelength) optically injects charge carriers into the sample via above-band gap excitation, and a subsequent THz pulse probes the conductivity of the

https://doi.org/10.1021/jacs.3c11172
J. Am. Chem. Soc. 2024, 146, 2574−2582

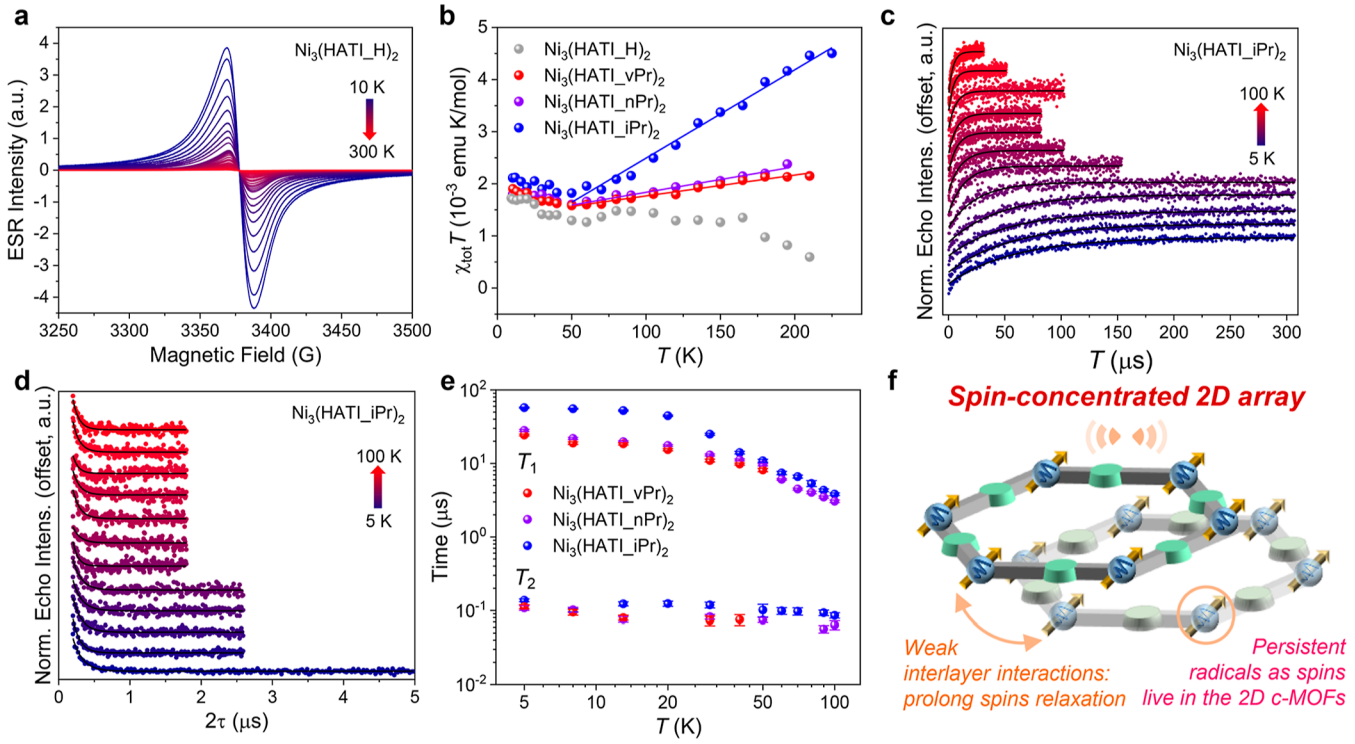

Figure 4. (a) VT-ESR spectra of $Ni_3(HATI\_H)_2$ at 10−300 K. (b) $\chi_{tot}T$ versus temperature (T) plot for the spin susceptibility (χ_{tot}) obtained from the double integration of the ESR spectra. The solid lines are fits using $\chi_{tot}T = C + \chi_{pauli}T$, where C and χ_{pauli} are the Curie constant and Pauli susceptibility. (c) Spin echo signal recovery for $Ni_3(HATI\_iPr)_2$ at different temperatures, from which T_1 is extracted using exponential fits (solid lines). (d) Hahn-echo decay for $Ni_3(HATI\_iPr)_2$ at different temperatures, from which T_2 is extracted using exponential fits (solid lines). (e) Temperature dependence of T_1 and T_2 for $Ni_3(HATI\_vPr)_2$, $Ni_3(HATI\_nPr)_2$, and $Ni_3(HATI\_iPr)_2$. (f) Schematic diagram of spin interaction and communication in 2D c-MOFs with highly staggered stacking.

photogenerated charge carriers, i.e., the photoconductivity $\Delta\sigma$: the pump-induced relative attenuation in the transmitted THz electric field $\left(-\frac{\Delta E}{E}\right)$ scales linearly with $\Delta\sigma$.[33] $\Delta\sigma$ is further related to the photogenerated charge-carrier density n (= the product of the free carrier generation quantum yield φ and absorbed photon density N_{abs}) and carrier mobility μ, following $\Delta\sigma = en\mu = e(\varphi N_{abs})\mu$. Figure 3c shows the THz photoconductivity dynamics of different samples divided to the absorbed photon density (N_{abs}): $\frac{\left(-\frac{\Delta E}{E}\right)}{N_{abs}} \propto \frac{\Delta\sigma}{N_{abs}} \propto \varphi\mu$. The photoconductivity per N_{abs} provides a direct comparison of the short-range carrier mobility (assuming a similar φ).

After photoexcitation, the photoconductivity dynamics exhibit a subpicosecond rise due to the formation of quasi-free charge carriers. This is followed by a decay process on the time scale of several ps. The subps fast photoconductivity decay and structure-independent lifetime (Figure S11) indicate that defect-assisted recombination is the dominant recombination mechanism.[34] This encourages further efforts to elucidate defect types, design approximate repair/passivation strategies, and conduct controlled spectroscopic studies, aiming to gain a deeper understanding of structure−property relationships, in particular, the role of interlayer distance and stacking structure on charge-carrier lifetime. As further elucidated in Figure 3d, the $\frac{\Delta\sigma}{N_{abs}}$ amplitude and thus the (relative) charge mobilities of the samples follow the following order: $Ni_3(HATI\_H)_2 > Ni_3(HATI\_vPr)_2 > Ni_3(HATI\_nPr)_2 > Ni_3(HATI\_iPr)_2$. This trend is in good agreement with the results of electrical conductivities, yet the variation in photoconductivity (factor of ∼2) is only a fraction of the conductivity variation (∼10^6). This is understandable since THz is sensitive primarily to short-range conductivity in the plane of 2D materials, while the conductivity measurements are limited by the less efficient out-of-plane transport. The modest variation in THz photoconductivity illustrates that chemical substitution of the 2D c-MOFs barely affects the in-plane conductivity but strongly affects the out-of-plane conductivity. The trend in THz photoconductivity can be explained qualitatively by band dispersion evolution, where increasing the steric bulkiness of side groups slightly weakens the in-plane band dispersion but highly suppresses the out-of-plane band dispersion (supported by DFT calculations discussed below). These results consistently suggest that the charge-carrier mobilities decrease with increasing the steric bulkiness of side groups by weakening the $\pi-\pi$ interactions between 2D layers and/or suppressing effective out-of-plane charge transport pathways.

In order to gain an in-depth understanding of the influence of stacking modes on the transport properties of $Ni_3(HATI\_X)_2$, DFT calculations are performed to predict the energy band diagrams for single-layer and layer-stacked 2D c-MOFs. The band structures of $Ni_3(HATI\_X)_2$ monolayers are almost not influenced by side group substitution (Figure S12), while the band gaps of bulk $Ni_3(HATI\_H)_2$, $Ni_3(HATI\_vPr)_2$, $Ni_3(HATI\_nPr)_2$, and $Ni_3(HATI\_iPr)_2$ can be deduced as 0.07, 0.26, 0.27, and 0.47 eV, respectively. In the case of $Ni_3(HATI\_H)_2$, the energy band near the Fermi level exhibits a dispersion of up to 0.5 eV (Figure 3e). In contrast, with increasing bulkiness of the side group, the

https://doi.org/10.1021/jacs.3c11172
J. Am. Chem. Soc. 2024, 146, 2574−2582

Table 1. Summary of Results Extracted from the Temperature Dependence of Spin Susceptibility

	spin density (10^{21}/mol)	C (10^{-3} emu K/mol)	n_{spin} (10^{21} cm^{-3})	χ_{Pauli} (10^{-5} emu/mol)	$\rho(E_F)$ (10^{22} eV^{-1} cm^{-3})
$Ni_3(HATI\_H)_2$	0.19				
$Ni_3(HATI\_vPr)_2$	1.89	1.37(5)	2.20(9)	0.40(2)	7.4(4)
$Ni_3(HATI\_nPr)_2$	2.50	1.35(3)	2.17(6)	0.49(2)	9.1(4)
$Ni_3(HATI\_iPr)_2$	5.96	0.80(8)	1.28(12)	1.69(5)	31.5(10)

corresponding energy band of $Ni_3(HATI\_iPr)_2$ shows a limited dispersion of only 0.05 eV (Figure 3f), indicating the increasingly localized nature of charge carriers (in line with electrical and THz results) and being almost on par with the band structures of monolayer 2D c-MOFs. These observations suggest that the interlayer electronic couplings in 2D c-MOFs strongly rely on the stacking modes, which not only influence the charge transport properties but also herald a significant impact on the spin communication between 2D layers (see below).

Spin Dynamic Behavior. The most basic information about a spin-concentrated molecular assembly revolves around the count of active spin centers it possesses.[19] Notably, these 2D c-MOFs possess identical topological networks and SBUs (the spins in 2D c-MOFs originated from the redox SBUs), which means that their spin densities should ideally be the same. The room-temperature spin densities of these 2D c-MOFs were quantified by electron spin resonance (ESR) measurements. Specifically, $Ni_3(HATI\_H)_2$, $Ni_3(HATI\_vPr)_2$, $Ni_3(HATI\_nPr)_2$, and $Ni_3(HATI\_iPr)_2$ possess spin densities of 1.9×10^{20}, 1.89×10^{21}, 2.50×10^{21}, and 5.96×10^{21} mol^{-1}, obtained by double integration of room-temperature ESR results, respectively. The 30-fold variation in the spin density of $Ni_3(HATI\_X)_2$ proves our design concept—successfully manipulating spin properties within the system through regulating 2D c-MOF stacking modes. The substitution of bulky groups (branched side chains) will dislocate the 2D layers and expand the interlayer distance, which spatially reduces the coupling between spins in different layers, resulting in a substantially higher spin density in $Ni_3(HATI\_iPr)_2$ than that in $Ni_3(HATI\_H)_2$.

VT-ESR measurements were then performed to elucidate the spin and transport properties of the 2D c-MOFs. The ESR spectra for $Ni_3(HATI\_H)_2$, $Ni_3(HATI\_vPr)_2$, and $Ni_3(HATI\_nPr)_2$ (Figures 4a and S13) consist of single components across the entire 10−300 K temperature range, where common g values of 2.0052, 2.0027, and 2.0020 were assigned, respectively. In striking contrast, $Ni_3(HATI\_iPr)_2$ exhibits asymmetric multicomponent spectra (Figure S13). Despite the unresolved broad peaks that preclude a satisfactory simulation of the spectra, this complex feature can be reasonably ascribed to the different types of organic radicals resulting from the staggered stacking of $Ni_3(HATI\_iPr)_2$. The ESR signal becomes weaker as the temperature rises in all cases, while this intensity decrease is more significant for $Ni_3(HATI\_H)_2$. Indeed, $Ni_3(HATI\_H)_2$ displays the weakest signal compared to the other samples at each measured temperature, notwithstanding its highest conductivity among them. This is likely because the carrier transport in these 2D c-MOFs is dominated by spinless polaron pairs or bipolarons.[35,36] In addition, this may also indicate the fast spin−lattice relaxation for $Ni_3(HATI\_H)_2$.[37,38] The temperature dependence of the ESR spectra is further analyzed in terms of their line widths (Figure S14), from which two temperature regions can be distinguished. At low temperatures (<100 K), the ESR line widths of the four samples decrease upon heating due to motional narrowing effects;[39] further elevating temperature leads to line broadening except for $Ni_3(HATI\_H)_2$. Spin−lattice relaxation facilitated by the Elliott mechanism is accountable for this observation,[38] which occurs by phonon scattering of metal-like conduction electrons, as previously evidenced in conducting polymers.[40]

To gain quantitative insights into these systems, the temperature dependence of spin susceptibility (χ_{tot}) was extracted from the double integration of the ESR spectra. The net susceptibility is written as the sum of the Pauli and Curie susceptibilities, $\chi_{tot} = \chi_{Pauli} + \chi_{Curie}$, referring to free and localized electrons, respectively. These two contributions can be better presented in a $\chi_{tot}T-T$ plot (Figures 4b and S15), being $\chi_{tot}T = \chi_{Pauli}T + C$, where C is the Curie constant.[41] For $Ni_3(HATI\_vPr)_2$, $Ni_3(HATI\_nPr)_2$, and $Ni_3(HATI\_iPr)_2$, clear slopes are observed in the temperature region 50−200 K, which indicates significant Pauli contributions from free conduction electrons (Table 1). The existence of free electrons makes the materials susceptible to the Elliott mechanism, which is consistent with the result of increased line widths at higher temperatures. On the contrary, $Ni_3(HATI\_H)_2$ with the highest conductivity shows almost constant $\chi_{tot}T$ values from 25 to 160 K, and thus, no noticeable line broadening is observed (Figure 4b). Overall, these analyses reveal that higher conductivity occurs when fewer free electrons are present in these 2D c-MOF samples (Table 1). This rather counterintuitive behavior has previously been reported[37,40] and confirms the previous hypothesis that electronic spin does not play a major role in carrier transport.

We conducted pulsed ESR measurements to further probe the spin dynamic properties of $Ni_3(HATI\_X)_2$ spin−lattice relaxation time (T_1) using spin−echo inversion recovery and spin−spin relaxation time (or quantum coherence time, T_2) using echo decay. Figure 4c,d portrays the experimental curves for $Ni_3(HATI\_iPr)_2$ as an example, from which the values of T_1 and T_2 are extracted by exponential fits below 100 K. The spin echo signal for $Ni_3(HATI\_H)_2$, however, is too weak to be recorded even at 5 K, indicative of the shortest T_1 and T_2 among these samples. Combined with the conductivities and temperature-dependent ESR results, the ultrashort spin−lattice relaxation time of $Ni_3(HATI\_H)_2$ could be attributed to the scattering of the metal-like conduction electrons by phonons. This may suggest that highly conductive 2D c-MOF systems are not necessarily good potential candidates for spin qubits. The results for the other three systems are illustrated in Figures 4e and S16: $Ni_3(HATI\_iPr)_2$ possesses higher T_1 values compared to those of $Ni_3(HATI\_nPr)_2$ and $Ni_3(HATI\_vPr)_2$. This should be due to the large interlayer distance and the mismatched stacking mode in $Ni_3(HATI\_iPr)_2$ with the most steric side group. This gives rise to an ultraweak interlayer interaction and hinders the lattice phonons, as demonstrated by the calculated electronic band dispersion.[30] Interestingly, the T_1 behavior of these materials is related to the Curie constant (C) and Pauli susceptibility (χ_{Pauli}) values extracted

https://doi.org/10.1021/jacs.3c11172
J. Am. Chem. Soc. 2024, 146, 2574−2582

from the VT-ESR results (Table 1). This tentatively suggests that more localized spins lead to longer T_1 values. Figure 4e reveals that T_2 is temperature-independent, and the values (~100 ns) are comparable among different samples, meaning that T_2 is not limited by thermally accelerated spin−lattice relaxation T_1. The latter may be explained by the fact that these samples consist of similar π-conjugated networks and nuclear spin baths and that communication between spins may mainly occur within the 2D layer (Figure 4f). The above results unravel that T_1 is dominated by the stacking modes of the 2D layer, with the looser packing (dislocated stacking and weak interlayer interaction) of 2D c-MOFs favoring longer spin−lattice relaxation time, while T_2 is independent of interlayer stacking. These systematical investigations of classical and quantum spin properties in these 2D c-MOFs provide a playground for studying the spin dynamics in spin-concentrated networks, where further improvements should be anticipated with the aim of excluding nuclear spin-rich atoms, such as nitrogen and hydrogen, while maintaining weak interlayer interactions.[42]

CONCLUSIONS

In conclusion, we have achieved precise and wide-range tuning of spin behavior, particularly with respect to the spin−lattice relaxation, in conductive 2D c-MOFs through control of the stacking mode. The π-conjugated hexaiminotriindole ligands attached by side groups with different shapes are synthesized, concomitant with precisely tunable stacking modes from serrated stacking to staggered stacking in corresponding 2D c-MOFs. Consequently, introducing bulky side group substitutions distinctly dislocates the stacking of 2D layers, attenuating the interlayer interactions within 2D c-MOFs. This perturbation yields a remarkable 30-fold enhancement in spin density and extends the lattice relaxation time of the spin carriers in the 2D c-MOFs. In these MOFs, the ability to control the stacking modes of the layers will also open up an avenue to discover the exotic physical properties of this class of van der Waals materials. Finally, a systematic investigation of the structure−property relation in these 2D c-MOFs lays a design guideline for offering spin qubits for QIS.

ASSOCIATED CONTENT

Supporting Information

The Supporting Information is available free of charge at https://pubs.acs.org/doi/10.1021/jacs.3c11172.

Experimental methods, characterization data, NMR spectra, TEM images, SEM images, XPS spectra, DFT calculations, conductivity measurements, terahertz spectroscopy, and EPR measurements (PDF)

AUTHOR INFORMATION

Corresponding Authors

Eugenio Coronado − *Instituto de Ciencia Molecular (ICMol), Universitat de València, 46980 Paterna, Spain;* orcid.org/0000-0002-1848-8791; Email: eugenio.coronado@uv.es

Renhao Dong − *Center for Advancing Electronics Dresden and Faculty of Chemistry and Food Chemistry, Technische Universität Dresden, 01067 Dresden, Germany; Key Laboratory of Colloid and Interface Chemistry of the Ministry of Education, School of Chemistry and Chemical Engineering, Shandong University, 250100 Jinan, China;* orcid.org/0000-0002-4125-9284; Email: renhaodong@sdu.edu.cn

Xinliang Feng − *Max Planck Institute of Microstructure Physics, 06120 Halle (Saale), Germany; Center for Advancing Electronics Dresden and Faculty of Chemistry and Food Chemistry, Technische Universität Dresden, 01067 Dresden, Germany;* orcid.org/0000-0003-3885-2703; Email: xinliang.feng@tu-dresden.de

Authors

Yang Lu − *Max Planck Institute of Microstructure Physics, 06120 Halle (Saale), Germany; Center for Advancing Electronics Dresden and Faculty of Chemistry and Food Chemistry, Technische Universität Dresden, 01067 Dresden, Germany; Université de Strasbourg, CNRS, ISIS, UMR 7006, 67000 Strasbourg, France*

Ziqi Hu − *Instituto de Ciencia Molecular (ICMol), Universitat de València, 46980 Paterna, Spain; Department of Materials Science and Engineering, CAS Key Laboratory of Materials for Energy Conversion, Anhui Laboratory of Advanced Photon Science and Technology, University of Science and Technology of China, 230026 Hefei, China*

Petko Petkov − *Faculty of Chemistry and Pharmacy, University of Sofia, 1164 Sofia, Bulgaria;* orcid.org/0000-0001-6315-8591

Shuai Fu − *Center for Advancing Electronics Dresden and Faculty of Chemistry and Food Chemistry, Technische Universität Dresden, 01067 Dresden, Germany; Max Planck Institute for Polymer Research, 55128 Mainz, Germany;* orcid.org/0000-0003-4038-2384

Haoyuan Qi − *Central Facility for Electron Microscopy, Electron Microscopy of Materials Science, Universität Ulm, 89081 Ulm, Germany*

Chuanhui Huang − *Center for Advancing Electronics Dresden and Faculty of Chemistry and Food Chemistry, Technische Universität Dresden, 01067 Dresden, Germany*

Yannan Liu − *Max Planck Institute of Microstructure Physics, 06120 Halle (Saale), Germany;* orcid.org/0000-0002-7379-3385

Xing Huang − *Max Planck Institute of Microstructure Physics, 06120 Halle (Saale), Germany*

Mingchao Wang − *Center for Advancing Electronics Dresden and Faculty of Chemistry and Food Chemistry, Technische Universität Dresden, 01067 Dresden, Germany;* orcid.org/0000-0001-9979-3503

Peng Zhang − *Center for Advancing Electronics Dresden and Faculty of Chemistry and Food Chemistry, Technische Universität Dresden, 01067 Dresden, Germany*

Ute Kaiser − *Central Facility for Electron Microscopy, Electron Microscopy of Materials Science, Universität Ulm, 89081 Ulm, Germany*

Mischa Bonn − *Max Planck Institute for Polymer Research, 55128 Mainz, Germany;* orcid.org/0000-0001-6851-8453

Hai I. Wang − *Max Planck Institute for Polymer Research, 55128 Mainz, Germany; Nanophotonics, Debye Institute for Nanomaterials Science, Utrecht University, 3584 CC Utrecht, The Netherlands;* orcid.org/0000-0003-0940-3984

Paolo Samorì − *Université de Strasbourg, CNRS, ISIS, UMR 7006, 67000 Strasbourg, France;* orcid.org/0000-0001-6256-8281

Complete contact information is available at: https://pubs.acs.org/10.1021/jacs.3c11172

Author Contributions

□These authors contributed equally. All authors have given approval to the final version of the manuscript.

Notes

The authors declare no competing financial interest.

■ ACKNOWLEDGMENTS

This work was financially supported by DFG projects (CRC-1415, no. 417590517; RTG 2861, no. 491865171), ERC starting grant (FC2DMOF, no. 852909), ERC Consolidator Grant (T2DCP, no. 819698), as well as the German Science Council and Center of Advancing Electronics Dresden (cfaed). R.D. thanks the National Natural Science Foundation of China (22272092), the Taishan Scholars Program of Shandong Province (tsqn201909047), and the Natural Science Foundation of Shandong Province (ZR2023JQ005). Y.L. and P.S. thank the Marie Skłodowska-Curie Fellowship T2DMOF (GA-101103585), the Interdisciplinary Thematic Institute SysChem via the IdEx Unistra (ANR-10-IDEX-0002) within the Investissement d'Avenir program, the Foundation Jean-Marie Lehn, and the Institut Universitaire de France (IUF). The authors acknowledge the cfaed and the Dresden Center for Nanoanalysis (DCN) at TUD. Y.L. acknowledges ZIH Dresden for computer time. P.P. is grateful to the European Union-NextGenerationEU, through the National Recovery and Resilience Plan of the Republic of Bulgaria, project no. BG-RRP-2.004-0008 for the financial support and Discoverer PetaSC and EuroHPC JU for awarding access to Discoverer supercomputer resources. We also appreciate help from Dr. Bin Han (Université de Strasbourg) on XPS measurements.

■ REFERENCES

(1) Lombardi, F.; Lodi, A.; Ma, J.; Liu, J.; Slota, M.; Narita, A.; Myers, W. K.; Mullen, K.; Feng, X.; Bogani, L. Quantum units from the topological engineering of molecular graphenoids. *Science* **2019**, *366* (6469), 1107−1110.

(2) Gaita-Ariño, A.; Luis, F.; Hill, S.; Coronado, E. Molecular spins for quantum computation. *Nat. Chem.* **2019**, *11* (4), 301−309.

(3) Atzori, M.; Sessoli, R. The Second Quantum Revolution: Role and Challenges of Molecular Chemistry. *J. Am. Chem. Soc.* **2019**, *141* (29), 11339−11352.

(4) Wasielewski, M. R.; Forbes, M. D. E.; Frank, N. L.; Kowalski, K.; Scholes, G. D.; Yuen-Zhou, J.; Baldo, M. A.; Freedman, D. E.; Goldsmith, R. H.; Goodson, T.; Kirk, M. L.; McCusker, J. K.; Ogilvie, J. P.; Shultz, D. A.; Stoll, S.; Whaley, K. B. Exploiting chemistry and molecular systems for quantum information science. *Nat. Rev. Chem* **2020**, *4* (9), 490−504.

(5) Coronado, E. Molecular magnetism: from chemical design to spin control in molecules, materials and devices. *Nat. Rev. Mater.* **2020**, *5* (2), 87−104.

(6) Hu, Z.; Dong, B. W.; Liu, Z.; Liu, J. J.; Su, J.; Yu, C.; Xiong, J.; Shi, D. E.; Wang, Y.; Wang, B. W.; Ardavan, A.; Shi, Z.; Jiang, S. D.; Gao, S. Endohedral Metallofullerene as Molecular High Spin Qubit: Diverse Rabi Cycles in Gd(2)@C(79)N. *J. Am. Chem. Soc.* **2018**, *140* (3), 1123−1130.

(7) Chen, X. X.; Li, J. T.; Fang, Y. H.; Deng, X. Y.; Wang, X. Q.; Liu, G.; Wang, Y.; Gu, X.; Jiang, S. D.; Lei, T. High-mobility semiconducting polymers with different spin ground states. *Nat. Commun.* **2022**, *13* (1), 2258.

(8) Jin, E.; Asada, M.; Xu, Q.; Dalapati, S.; Addicoat, M. A.; Brady, M. A.; Xu, H.; Nakamura, T.; Heine, T.; Chen, Q.; Jiang, D. Two-dimensional sp(2) carbon-conjugated covalent organic frameworks. *Science* **2017**, *357* (6352), 673−676.

(9) Wang, S.-J.; Venkateshvaran, D.; Mahani, M. R.; Chopra, U.; McNellis, E. R.; Di Pietro, R.; Schott, S.; Wittmann, A.; Schweicher, G.; Cubukcu, M.; Kang, K.; Carey, R.; Wagner, T. J.; Siebrecht, J. N. M.; Wong, D. P. G. H.; Jacobs, I. E.; Aboljadayel, R. O.; Ionescu, A.; Egorov, S. A.; Mueller, S.; Zadvorna, O.; Skalski, P.; Jellett, C.; Little, M.; Marks, A.; McCulloch, I.; Wunderlich, J.; Sinova, J.; Sirringhaus, H. Long spin diffusion lengths in doped conjugated polymers due to enhanced exchange coupling. *Nat. Electron.* **2019**, *2* (3), 98−107.

(10) Szulczewski, G.; Sanvito, S.; Coey, M. A spin of their own. *Nat. Mater.* **2009**, *8* (9), 693.

(11) Dai, Y. Z.; Dong, B. W.; Kao, Y.; Wang, Z. Y.; Un, H. I.; Liu, Z.; Lin, Z. J.; Li, L.; Xie, F. B.; Lu, Y.; Xu, M. X.; Lei, T.; Sun, Y. J.; Wang, J. Y.; Gao, S.; Jiang, S. D.; Pei, J. Chemical Modification toward Long Spin Lifetimes in Organic Conjugated Radicals. *ChemPhysChem* **2018**, *19* (22), 2972−2977.

(12) Wang, Z.-Y.; Dai, Y.-Z.; Yao, Z.-F.; Dong, B.-W.; Lu, Y.; Ding, L.; Jiang, S.-D.; Wang, J.-Y.; Pei, J. Conformation-Dependent Spin Relaxation Behaviors of 6-Oxoverdazyl Radical Single Crystals. *Cryst. Growth Des.* **2020**, *20* (4), 2141−2146.

(13) Slota, M.; Keerthi, A.; Myers, W. K.; Tretyakov, E.; Baumgarten, M.; Ardavan, A.; Sadeghi, H.; Lambert, C. J.; Narita, A.; Mullen, K.; Bogani, L. Magnetic edge states and coherent manipulation of graphene nanoribbons. *Nature* **2018**, *557* (7707), 691−695.

(14) Wang, M.; Dong, R.; Feng, X. Two-dimensional conjugated metal-organic frameworks (2D c-MOFs): chemistry and function for MOFtronics. *Chem. Soc. Rev.* **2021**, *50* (4), 2764−2793.

(15) Xie, L. S.; Skorupskii, G.; Dinca, M. Electrically Conductive Metal-Organic Frameworks. *Chem. Rev.* **2020**, *120* (16), 8536−8580.

(16) Ko, M.; Mendecki, L.; Mirica, K. A. Conductive two-dimensional metal-organic frameworks as multifunctional materials. *Chem. Commun.* **2018**, *54* (57), 7873−7891.

(17) Sakamoto, R.; Fukui, N.; Maeda, H.; Toyoda, R.; Takaishi, S.; Tanabe, T.; Komeda, J.; Amo-Ochoa, P.; Zamora, F.; Nishihara, H. Layered metal-organic frameworks and metal-organic nanosheets as functional materials. *Coord. Chem. Rev.* **2022**, *472*, 214787.

(18) Huang, X.; Sheng, P.; Tu, Z.; Zhang, F.; Wang, J.; Geng, H.; Zou, Y.; Di, C. A.; Yi, Y.; Sun, Y.; Xu, W.; Zhu, D. A two-dimensional pi-d conjugated coordination polymer with extremely high electrical conductivity and ambipolar transport behaviour. *Nat. Commun.* **2015**, *6*, 7408.

(19) Oanta, A. K.; Collins, K. A.; Evans, A. M.; Pratik, S. M.; Hall, L. A.; Strauss, M. J.; Marder, S. R.; D'Alessandro, D. M.; Rajh, T.; Freedman, D. E.; Li, H.; Bredas, J. L.; Sun, L.; Dichtel, W. R. Electronic Spin Qubit Candidates Arrayed within Layered Two-Dimensional Polymers. *J. Am. Chem. Soc.* **2023**, *145* (1), 689−696.

(20) Sun, L.; Yang, L.; Dou, J. H.; Li, J.; Skorupskii, G.; Mardini, M.; Tan, K. O.; Chen, T.; Sun, C.; Oppenheim, J. J.; Griffin, R. G.; Dinca, M.; Rajh, T. Room-Temperature Quantitative Quantum Sensing of Lithium Ions with a Radical-Embedded Metal-Organic Framework. *J. Am. Chem. Soc.* **2022**, *144* (41), 19008−19016.

(21) Zadrozny, J. M.; Gallagher, A. T.; Harris, T. D.; Freedman, D. E. A Porous Array of Clock Qubits. *J. Am. Chem. Soc.* **2017**, *139* (20), 7089−7094.

(22) Fan, K.; Zhang, C.; Chen, Y.; Wu, Y.; Wang, C. The chemical states of conjugated coordination polymers. *Chem.* **2021**, *7* (5), 1224−1243.

(23) Yamabayashi, T.; Atzori, M.; Tesi, L.; Cosquer, G.; Santanni, F.; Boulon, M. E.; Morra, E.; Benci, S.; Torre, R.; Chiesa, M.; Sorace, L.; Sessoli, R.; Yamashita, M. Scaling Up Electronic Spin Qubits into a Three-Dimensional Metal-Organic Framework. *J. Am. Chem. Soc.* **2018**, *140* (38), 12090−12101.

(24) Sheberla, D.; Sun, L.; Blood-Forsythe, M. A.; Er, S.; Wade, C. R.; Brozek, C. K.; Aspuru-Guzik, A.; Dinca, M. High electrical conductivity in Ni(3)(2,3,6,7,10,11-hexaiminotriphenylene)(2), a semiconducting metal-organic graphene analogue. *J. Am. Chem. Soc.* **2014**, *136* (25), 8859−8862.

(25) Choi, J. Y.; Stodolka, M.; Kim, N.; Pham, H. T.; Check, B.; Park, J. 2D conjugated metal-organic framework as a proton-electron dual conductor. *Chem.* **2023**, *9* (1), 143−153.

https://doi.org/10.1021/jacs.3c11172
J. Am. Chem. Soc. 2024, 146, 2574−2582

(26) Dou, J. H.; Arguilla, M. Q.; Luo, Y.; Li, J.; Zhang, W.; Sun, L.; Mancuso, J. L.; Yang, L.; Chen, T.; Parent, L. R.; Skorupskii, G.; Libretto, N. J.; Sun, C.; Yang, M. C.; Dip, P. V.; Brignole, E. J.; Miller, J. T.; Kong, J.; Hendon, C. H.; Sun, J.; Dinca, M. Atomically precise single-crystal structures of electrically conducting 2D metal-organic frameworks. *Nat. Mater.* **2021**, *20* (2), 222−228.
(27) Lu, Y.; Zhong, H.; Li, J.; Dominic, A. M.; Hu, Y.; Gao, Z.; Jiao, Y.; Wu, M.; Qi, H.; Huang, C.; Wayment, L. J.; Kaiser, U.; Spiecker, E.; Weidinger, I. M.; Zhang, W.; Feng, X.; Dong, R. sp-Carbon Incorporated Conductive Metal-Organic Framework as Photocathode for Photoelectrochemical Hydrogen Generation. *Angew. Chem., Int. Ed.* **2022**, *61*, No. e202208163.
(28) Meng, Z.; Jones, C. G.; Farid, S.; Khan, I. U.; Nelson, H. M.; Mirica, K. A. Unraveling the Electrical and Magnetic Properties of Layered Conductive Metal-Organic Framework With Atomic Precision. *Angew. Chem., Int. Ed.* **2022**, *61* (6), No. e202113569.
(29) Qi, M.; Zhou, Y.; Lv, Y.; Chen, W.; Su, X.; Zhang, T.; Xing, G.; Xu, G.; Terasaki, O.; Chen, L. Direct Construction of 2D Conductive Metal-Organic Frameworks from a Nonplanar Ligand: In Situ Scholl Reaction and Topological Modulation. *J. Am. Chem. Soc.* **2023**, *145* (5), 2739−2744.
(30) Yu, C. J.; von Kugelgen, S.; Krzyaniak, M. D.; Ji, W.; Dichtel, W. R.; Wasielewski, M. R.; Freedman, D. E. Spin and Phonon Design in Modular Arrays of Molecular Qubits. *Chem. Mater.* **2020**, *32* (23), 10200−10206.
(31) Tang, W.-Q.; Zhao, Y.-J.; Xu, M.; Xu, J.-Y.; Meng, S.-S.; Yin, Y.-D.; Zhang, Q.-H.; Gu, L.; Liu, D.-H.; Gu, Z.-Y. Controlling the Stacking Modes of Metal-Organic Framework Nanosheets through Host-Guest Noncovalent Interactions. *Angew. Chem., Int. Ed.* **2021**, *60* (13), 6920−6925.
(32) Kang, C.; Zhang, Z.; Wee, V.; Usadi, A. K.; Calabro, D. C.; Baugh, L. S.; Wang, S.; Wang, Y.; Zhao, D. Interlayer Shifting in Two-Dimensional Covalent Organic Frameworks. *J. Am. Chem. Soc.* **2020**, *142* (30), 12995−13002.
(33) Ulbricht, R.; Hendry, E.; Shan, J.; Heinz, T. F.; Bonn, M. Carrier dynamics in semiconductors studied with time-resolved terahertz spectroscopy. *Rev. Mod. Phys.* **2011**, *83* (2), 543−586.
(34) Jin, E.; Fu, S.; Hanayama, H.; Addicoat, M. A.; Wei, W.; Chen, Q.; Graf, R.; Landfester, K.; Bonn, M.; Zhang, K. A. I.; Wang, H. I.; Mullen, K.; Narita, A. A Nanographene-Based Two-Dimensional Covalent Organic Framework as a Stable and Efficient Photocatalyst. *Angew. Chem., Int. Ed.* **2022**, *61* (5), No. e202114059.
(35) Heeger, A. J. Semiconducting polymers: the Third Generation. *Chem. Soc. Rev.* **2010**, *39* (7), 2354−2371.
(36) Bubnova, O.; Khan, Z. U.; Wang, H.; Braun, S.; Evans, D. R.; Fabretto, M.; Hojati-Talemi, P.; Dagnelund, D.; Arlin, J. B.; Geerts, Y. H.; Desbief, S.; Breiby, D. W.; Andreasen, J. W.; Lazzaroni, R.; Chen, W. M.; Zozoulenko, I.; Fahlman, M.; Murphy, P. J.; Berggren, M.; Crispin, X. Semi-metallic polymers. *Nat. Mater.* **2014**, *13* (2), 190−194.
(37) Tanaka, H.; Hirate, M.; Watanabe, S.; Kuroda, S. i. Microscopic signature of metallic state in semicrystalline conjugated polymers doped with fluoroalkylsilane molecules. *Adv. Mater.* **2014**, *26* (15), 2376−2383.
(38) Elliott, R. J. Theory of the effect of spin-orbit coupling on magnetic resonance in some semiconductors. *Phys. Rev.* **1954**, *96* (2), 266−279.
(39) Matsui, H.; Kumaki, D.; Takahashi, E.; Takimiya, K.; Tokito, S.; Hasegawa, T. Correlation between interdomain carrier hopping and apparent mobility in polycrystalline organic transistors as investigated by electron spin resonance. *Phys. Rev. B: Condens. Matter Mater. Phys.* **2012**, *85* (3), 035308.
(40) Lu, Y.; Yu, Z. D.; Un, H. I.; Yao, Z. F.; You, H. Y.; Jin, W.; Li, L.; Wang, Z. Y.; Dong, B. W.; Barlow, S.; et al. Persistent Conjugated Backbone and Disordered Lamellar Packing Impart Polymers with Efficient n-Doping and High Conductivities. *Adv. Mater.* **2021**, *33* (2), 2005946.
(41) Kang, K.; Watanabe, S.; Broch, K.; Sepe, A.; Brown, A.; Nasrallah, I.; Nikolka, M.; Fei, Z.; Heeney, M.; Matsumoto, D.; et al. 2D coherent charge transport in highly ordered conducting polymers doped by solid state diffusion. *Nat. Mater.* **2016**, *15* (8), 896−902.
(42) Zadrozny, J. M.; Niklas, J.; Poluektov, O. G.; Freedman, D. E. Millisecond Coherence Time in a Tunable Molecular Electronic Spin Qubit. *ACS Cent. Sci.* **2015**, *1* (9), 488−492.

https://doi.org/10.1021/jacs.3c11172
J. Am. Chem. Soc. 2024, 146, 2574−2582